ORIGINAL ARTICLE

Journal
of the American Ceramic Society

Band gap narrowing and magnetic properties of transition-metal-doped $Ba_{0.85}Ca_{0.15}Ti_{0.9}Zr_{0.1}O_3$ lead-free ceramics

Yuemin Zhang[1] | Hongmei Deng[2] | Shufang Si[1] | Tiantian Wang[1] |
Dongliang Zheng[1] | Pingxiong Yang[1] | Junhao Chu[1]

[1]Key Laboratory of Polar Materials and Devices, Ministry of Education, School of Communication and Electronic Engineering, School of Physics and Electronic Science, East China Normal University, Shanghai, People's Republic of China

[2]Instrumental Analysis and Research Center, Institute of Materials, Shanghai University, Shanghai, People's Republic of China

Correspondence
Pingxiong Yang, Key Laboratory of Polar Materials and Devices, Ministry of Education, School of Communication and Electronic Engineering, School of Physics and Electronic Science, East China Normal University, Shanghai 200241, People's Republic of China.
Email: pxyang@ee.ecnu.edu.cn

Funding information
National Natural Science Foundation of China, Grant/Award Number: 61474045

Abstract

Transition metal (TM = Mn, Fe, Co, and Ni)-doped $Ba_{0.85}Ca_{0.15}Ti_{0.9}Zr_{0.1}O_3$ (BCZT) lead-free ceramics with excellent optical and magnetic properties are synthesized via a solid-state reaction method. The effects of TM elements on the sintering, structure, optical, and magnetic properties of BCZT ceramics are investigated in detail. Structural phase transition from the coexistence of rhombohedral and tetragonal phases to a single rhombohedral phase is observed owing to grain refinement. A narrow band gap of 1.68 eV is achieved in the Co-doped BCZT. The optical absorption of TM-doped BCZT is enhanced, which is ascribed to the molecular orbital rearrangement caused by lattice distortion. Moreover the magnetic behaviors of TM-doped BCZT are observed. The Fe-doped BCZT presents the most evident ferromagnetism, resulting from the exchange coupling interaction between the Fe^{3+} ions and oxygen vacancies. These results provide additional insight into the use of TM-doped BCZT lead-free ferroelectric ceramics for various applications.

KEYWORDS
band gap, BCZT, lead-free ceramics, magnetic properties, phase transition

1 | INTRODUCTION

Perovskite ferroelectric materials have received increasing research attention owing to their promising electrical, mechanical, thermal, magnetic, optical, and other properties.[1,2] Traditional lead-based perovskite materials, such as $PbTiO_3$ (PTO) and $PbZr_xTi_{1-x}O_3$ (PZT),[3,4] are well known for their outstanding electrical properties, but also arouse great concerns as their excessive lead content causes significant harm to the human body and environment. Consequently, the development and utilization of lead-free materials have been promoted.[5,6] For the past few years, considerable attention has been paid to lead-free perovskite ceramics, which can be classified into three main categories as follows: $K_{0.5}Na_{0.5}NbO_3$ (KNN), $Bi_{0.5}Na_{0.5}TiO_3$ (BNT), and $BaTiO_3$ (BT).[7–9] Liu and Ren[10] recently reported an excellent lead-free ceramic, that is, $0.5Ba(Ti_{0.8}Zr_{0.2})O_3$–$0.5(Ba_{0.7}Ca_{0.3})TiO_3$ (BCZT) with a morphotropic phase boundary between the rhombohedral and tetragonal phases; its piezoelectric coefficient d_{33} (620 pC/N) was even greater than that of soft PZT.

Compared with pure BCZT, doped BCZT may have better physical properties. For instance, Sun et al[11] reported that Mn-doped BCZT ceramic (0.3 mol%) had excellent ferroelectric ($P_r = 15.7$ μC/cm², $E_c = 180$ V/mm), dielectric (tan$\delta = 1.04$%), and piezoelectric ($d_{33} = 308$ pC/N) properties. Jaimeewong et al[12] also observed favorable dielectric ($\varepsilon_r = 4567$) and piezoelectric ($d_{33} = 276$ pC/N) properties in CoO- and Fe_2O_3-doped BCZT ceramics. In addition, owing to their excellent dielectric energy storage performance, $BaTiO_3$-based materials are of great value in memory and transformer applications and can also be applied to high-temperature capacitors and pulsed power.[13–15]

Novel photovoltaic materials with perovskite structures are being intensively studied.[16,17] Based on the bulk photovoltaic effect, the spontaneous polarization of ferroelectric ABO_3 perovskite materials facilitates the separation of photoexcited carriers and enables voltages higher than the band gap.[18,19] Nevertheless, similar to traditional ferroelectrics, BCZT has a wide band gap beyond 3.0 eV and large absorption in the ultraviolet region. Recent studies have observed that the introduction of transition metal (TM) elements into the B-site of PTO perovskite significantly reduces the band gap, because TM elements have fewer ionic bonds and more covalent bonds with oxygen.[20] Moreover an optimized concentration of TM ions in PTO perovskite can enhance its magnetization.[21]

Thus far, very few studies have been conducted on the optical and magnetic properties of BCZT ferroelectric materials. For instance, Zheng et al[22] reported the improved optical and magnetic properties of PTO ceramics by doping with 5 mol% Fe; Yu et al[23] achieved a narrower band gap and greater saturated magnetization in $Bi_{0.9}Sm_{0.1}FeO_3$ by doping with 5 mol% Mn and 5 mol% Ni. Thus, we can expect controllable optical and magnetic properties in the previously mentioned BCZT materials if TM doping is applied. In this work, we investigate the structural, optical, and magnetic properties of TM (Mn, Fe, Co, and Ni)-doped BCZT ceramics using a conventional solid-state reaction method. The results suggest that BCZT lead-free ceramics have immense potential in the fields of optoelectronics and multifunctional materials.

2 | EXPERIMENTAL PROCEDURES

$Ba_{0.85}Ca_{0.15}(Ti_{0.9}Zr_{0.1})_{0.95}TM_{0.05}O_3$ (BCZT–0.05TM) ceramics with TM = Mn, Fe, Co, and Ni (abbr. BCZTM, BCZTF, BCZTC, and BCZTN, respectively) were synthesized via a solid-state reaction method. The starting materials $BaCO_3$ (99%), TiO_2 (99%), CaO (98%), ZrO_2 (99%), MnO (99.5%), Fe_2O_3 (99%), CoO (99%), and NiO (99%) were weighed in a stoichiometric amount and ball-milled for 12 hours in an ethanol medium containing zirconia balls. The dried slurries were first calcined at 900°C for 4 hours. To improve the efficiency of heat absorption further, the resulting powders were reground for 8 hours, granulated with 5 wt% polyvinyl alcohol subsequently, and uniaxially pressed into cylindrical pellets of diameter 10 mm and thickness 1-2 mm. Finally, the pellets were sintered at the optimum temperature of 1400°C for 4 hours in covered alumina crucibles. As a reference, pure BCZT ceramic was also prepared under the same conditions.

The phase purity and structure of the BCZT ceramics were identified using X-ray diffraction (XRD) with Cu K_α radiation (Bruker D8 Advance, $\lambda = 0.154056$ nm) and Raman spectroscopy (Renishaw plc InVia plus, 514.5 nm). The surface morphologies and grain size were observed using scanning electron microscopy (SEM, Philips XL30FEG). The optical absorbance was determined using ultraviolet–visible–near-infrared (UV-vis-NIR) spectrophotometry (Cary500, USA Varian). The magnetic properties were measured using a physical property measurement system (PPMS-9, Quantum Design). All the measurements were obtained at room temperature.

3 | RESULTS AND DISCUSSIONS

Figure 1A shows the XRD patterns of the BCZT and BCZT–0.05TM ferroelectric polycrystalline ceramics in the 2θ range of 10°-70°. All the BCZT ceramics exhibit a polycrystalline perovskite structure with apparent peaks of (100), (110), (111), (002), (221), and (210), similar to a previous report. Notice that no peaks from the impurity

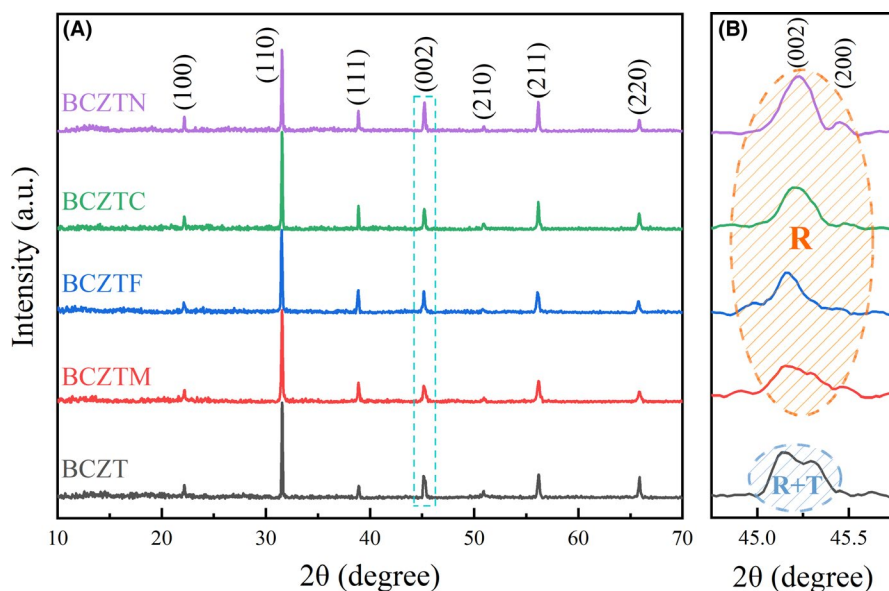**FIGURE 1** A, XRD patterns of BCZT and BCZT–0.05TM (TM = Mn, Fe, Co, and Ni) ceramics. B, Magnified patterns in the 2θ range of 44.5°-46°

phases, for example, MnO, Fe_2O_3, CoO, and NiO, can be detected.[24] As shown in Figure 1B, the fine-scanned XRD patterns in the 2θ range of 44.5°-46° illustrate the coexistence of rhombohedral (R, R3m, PDF#85-1797) and tetragonal (T, P4mm, PDF#05-0626) phases in the undoped BCZT ceramic.[25] However, with TM cation doping, the peaks of (200) are weakened, indicating the phase transition from the T phase to the R phase. There are still mixed phases in BCZTM, whereas only the R phase is observed in BCZTF, BCZTC, and BCZTN ceramics.[26] It is expected that ions with radius less than 0.870 Å such as Mn^{2+} (0.670 Å), Fe^{3+} (0.645 Å), Co^{2+} (0.745 Å), and Ni^{2+} (0.690 Å) will occupy the B-site,[12] which may induce contraction of the lattice. In addition, oxygen vacancies caused by charge imbalance promote lattice shrinkage.[23] The corresponding lattice parameters and cell densities are shown in Table 1. It can be observed that the lattice parameters of the doped BCZT ceramics are reduced, and their densities are larger than that of undoped BCZT. These results demonstrate that the radius effects and oxygen vacancies induced by doping promote the phase evolution.

To explore the structure and phase purity of BCZT ceramics further, Raman characterization was conducted owing to its sensitivity to the structural symmetry. Figure 2 shows the Raman spectra of BCZT samples measured within the range of 100-1000 cm^{-1}. The Raman spectrum of the pure BCZT ceramic includes a broad peak centered at ~190 cm^{-1}, a weak shoulder peak at ~292 cm^{-1}, an asymmetric peak at ~530 cm^{-1}, and a broad weak peak at ~740 cm^{-1}. According to previous reports, these peaks can be assigned to the $A_1(TO)$, B_1,E(TO + LO), A_1,E(TO), and A_1,E(LO) phonon modes, respectively.[27] The peaks at ~530 and ~740 cm^{-1} match the phonon vibrations of Ba–O bonds, and the peaks in the range of 190-290 cm^{-1} accord with the phonon vibrations of Ti–O bonds.[28] The aforementioned peaks confirm the existence of the tetragonal phase of BCZT ceramics, which resembles that of $BaTiO_3$-based materials.[29] The phase structures of TM-doped BCZT ceramics are similar to that of pure BCZT, except for the peak intensity, width, and

position, which have some differences. In pure BCZT, the broad peak of the $A_1(TO)$ mode at ~190 cm^{-1} is the signature of the T ferroelectric phase, and the peak at ~292 cm^{-1} confirms the coexistence of the T and R phases. In the doped BCZT, the peaks at ~190 cm^{-1} are weakened and the peaks beyond 290 cm^{-1} become sharp, which is attributed to the phase transition from the T phase to the R phase.[30] The modes around 530 cm^{-1} are mainly derived from the vibrations of oxygen displacements, and the modes beyond 700 cm^{-1} are known to correlate with the presence of oxygen vacancies. In BCZTM and BCZTC, the peaks at ~ 700 cm^{-1} are sharp, which may originate from the defects induced by Mn and Co doping.[31] Moreover the asymmetry and disorder of the crystal structure can be inferred from the broadening and offset of Raman spectra, which are caused by the phase transition.[32]

The SEM images of the sintered BCZT ceramics, as shown in Figure 3, further demonstrate the surface morphologies. The microstructures of the pure BCZT ceramic exhibit a relatively large grain size and clear grain boundary without evident agglomeration. The grain size decreases evidently and becomes less uniform with TM cation doping. Grain refinement occurs owing to the doping of TM elements, which inhibits grain growth in the grain boundary. Similar growth mechanisms have also been observed in Ni-doped $PbTiO_3$, Co-doped $BaTiO_3$, and Fe-doped $BiYbO_3$–Pb(Zr,Ti)O_3.[17,33,34] Additionally, the increment in the relative density can be attributed to the oxygen vacancies produced by acceptor dopants, which are conducive to mass transfer.[35]

Figure 4 illustrates the UV-vis-NIR optical absorption spectra of the fine BCZT powders in the wavelength region of 200-1200 nm, which are derived from the reflection spectra according to the Kubelka-Munk (K-M) function:

$$F(R) = \frac{(1-R)^2}{2R}$$

Here R is the reflectivity corresponding to the $BaSO_4$ standard, and the absorption coefficient (α) is proportional to $F(R)$. As shown in Figure 4A, the pure BCZT ceramic exhibits a

TABLE 1 Lattice parameters, unit cell volume, and densities of BCZT and BCZT–0.05TM ceramics

Composition	Space group	a, b, c [Å]	Cell volume V [Å^3]	Density
BCZT	P4mm + R3m	$a = b = 4.01168$ $c = 4.00218$	64.41	6.0052
		$a = b = c = 4.01173$	64.56	
BCZTM	P4mm + R3m	$a = b = 4.01022$ $c = 4.00458$	64.40	6.0122
		$a = b = c = 4.00888$	64.42	
BCZTF	R3m	$a = b = c = 4.00288$	64.20	6.0324
BCZTC	R3m	$a = b = c = 4.00680$	64.33	6.0201
BCZTN	R3m	$a = b = c = 4.00639$	64.31	6.0220

broad absorption below 400 nm, which is due to the transition of the carriers from the valence band to the conduction band. Subsequently, the absorbance descends steeply at 400 nm. By contrast, in the case of TM cation doping, the BCZT–0.05TM ceramics exhibit a wider absorption range in the visible region. The changes in the absorption spectra are strongly associated with the optical band gap (E_g) of the BCZT samples, which can be deduced from the tangent in the Tauc plot as expressed below:

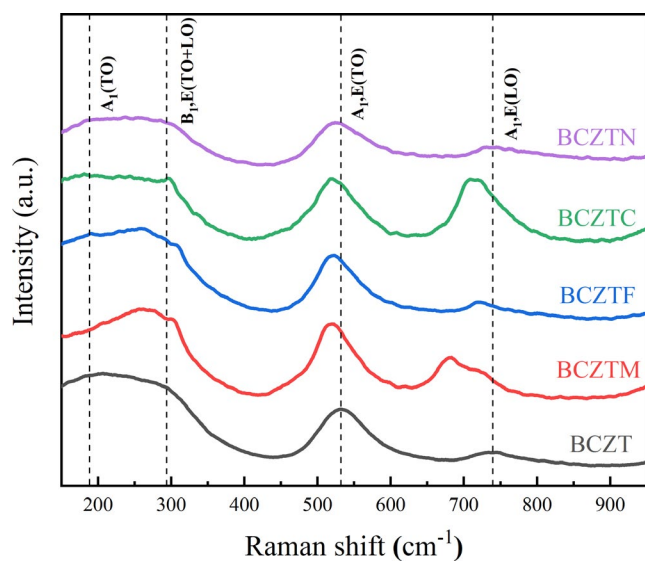$$(\alpha h\nu)^n = A\left(h\nu - E_g\right)$$

FIGURE 2 Room-temperature Raman spectra of BCZT and BCZT–0.05TM ceramics

where $h\nu$ is the photon energy, A is a proportional constant, and n = 2 and 1/2 for the direct and indirect allowed transitions, respectively.[36] Ma et al[20] reported that the band gap of BCZT was direct, by fitting the K–M function with the Tauc function. Therefore, we consider n = 2 in all the Tauc functions for BCZT. As demonstrated in Figure 4B, the E_g values of BCZTM, BCZTF, BCZTC, and BCZTN obtained by extrapolating the linear part to the horizontal axis are 1.95, 2.26, 1.68, and 3.04 eV, respectively, which are considerably lower than that of the pure BCZT (3.18 eV). Among them, the band gap reduction of BCZTC is the most evident, and is even more significant than those of other photovoltaic perovskite ceramics.[35,37,38]

These optical behaviors can be explained by the newly emerging electronic states of the highest occupied molecular orbital (HOMO) and the lowest unoccupied molecular orbital (LUMO) generated by TM cation doping. In BCZT, the HOMO is around the O/2p orbital, which has a slight interaction with the Ti/3d and Ba/6p orbitals, whereas the LUMO is around the Ti/3d orbital.[17] The position of the conduction band depends on the electronegativity of the doping ions; the greater the electronegativity of the ions, the lower is the conduction band.[39] When the doping element is introduced, the HOMO is localized around the TM/3d orbital. As the TM cations are more electronegative than Ti, the energy of the TM/3d orbital is lower than that of the Ti/3d orbital. Consequently, there is a downward shift of the conduction band edge into the band gap, resulting in the reduction of E_g. Moreover according to Choi's report,[40] in addition to electronegativity, the optical band gap may be related to the lattice distortion caused by the ion substitution The lattice distortion increases as the radius of the doping
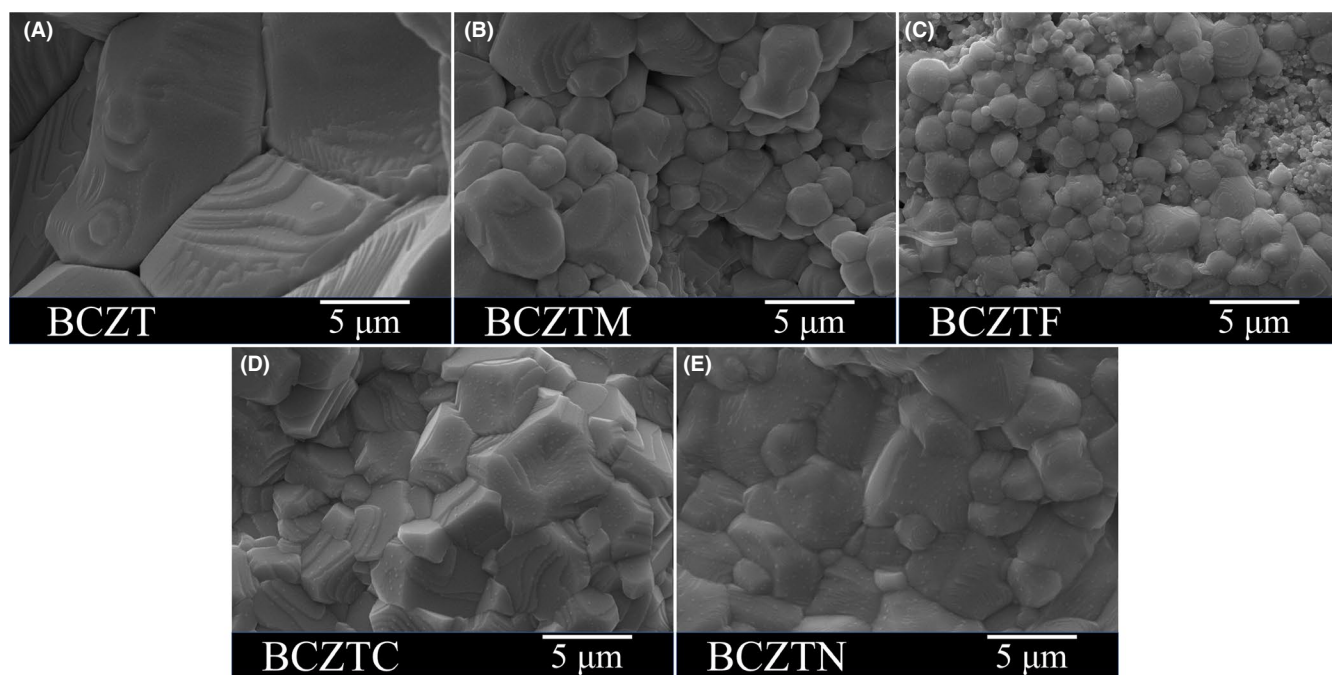

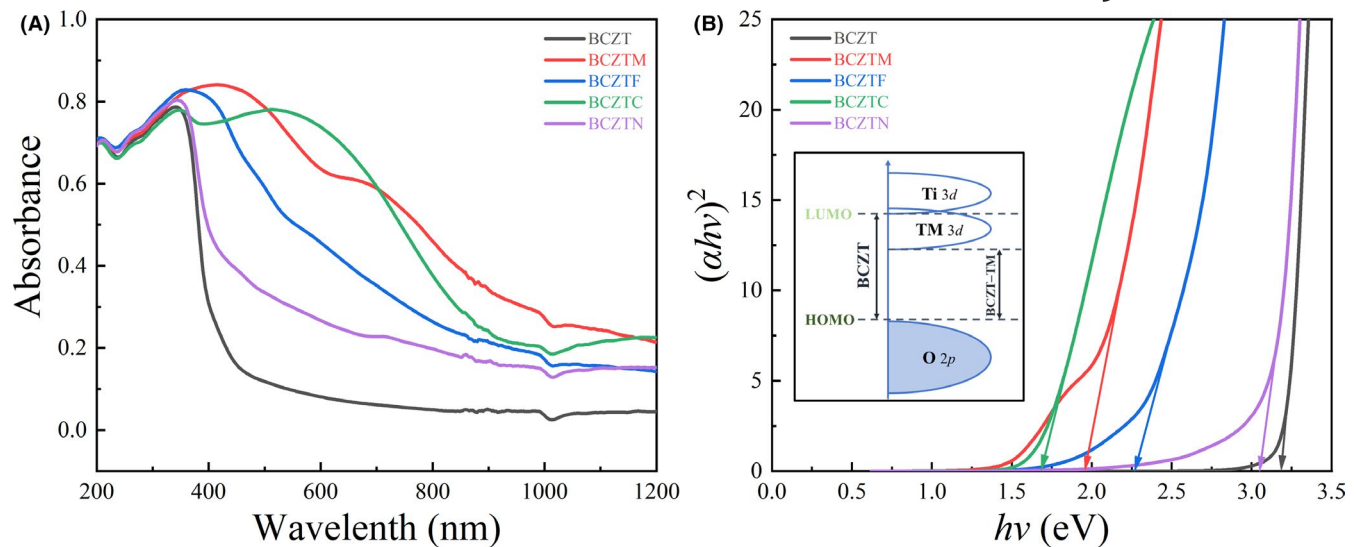**FIGURE 3** SEM images of the surface for the ceramics: A, BCZT, B, BCZTM, C, BCZTF, D, BCZTC, and E, BCZTN

FIGURE 4 A, UV-vis-NIR absorption spectra of the as-synthesized ceramics. B, Plots of $(\alpha h\nu)^2$ vs $h\nu$ for the absorption spectra. The inset shows a schematic diagram of the mechanism for band gap narrowing

FIGURE 5 *M-H* curves of the ceramics at room temperature: (A) BCZT, (B) BCZTM, (C) BCZTF, and the zoomed-in images in the inset, (D) BCZTC, (E) BCZTN. (F) Schematic diagram of magnetic polarons in the case of Fe^{3+} doping
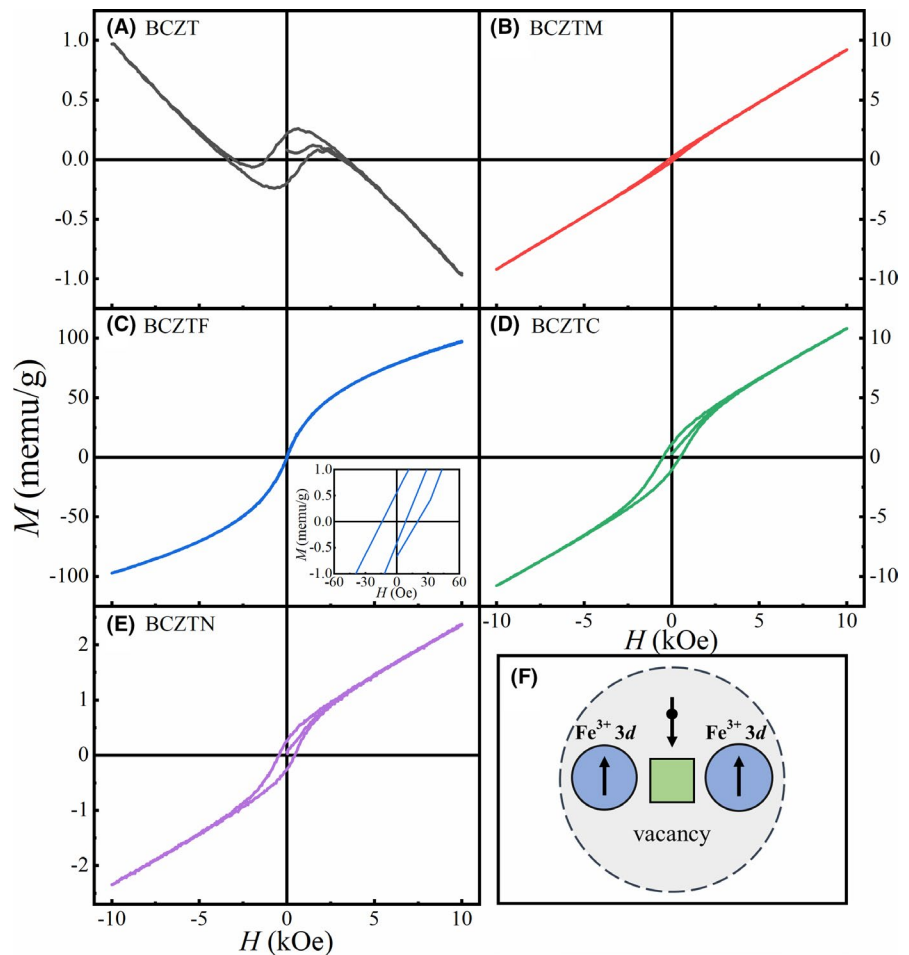
ions decreases, which leads to a rearrangement of the molecular orbital and a reduction in the band gap. According to the experimental data analysis, Co may be the preferred element to reduce the band gap of BCZT. These results indicate that we can effectively reduce the band gap of BCZT ceramics via TM doping to improve their properties for visible and ultraviolet absorption. We believe that optimizing the doping concentration can further modify the band gap of BCZT materials, and

Composition	Remanent magnetization M_r (memu/g)	Coercive field H_c (Oe)	Saturation magnetization M_s (memu/g)
BCZT	—	—	0
BCZTM	0.18	128	9.22
BCZTF	0.56	20	97.42
BCZTC	1.09	485	10.80
BCZTN	0.25	461	2.37

TABLE 2 Remanent magnetization, coercive field, and saturation magnetization values of BCZT and BCZT–0.05TM ceramics

even match the optimal band gap for application to solar cell materials.

The magnetic measurements of the magnetization vs magnetic field (*M-H*) curves of the BCZT powders were performed with a maximum magnetic field of 10 kOe at room temperature; the results are illustrated in Figure 5A-E. For the undoped BCZT in Figure 5A, there is an anti-S-type *M-H* curve, indicating the natural diamagnetism of BCZT. For the Mn-doped BCZT in Figure 5B, a linear *M-H* curve is observed owing to the antiferromagnetism of Mn. In comparison, the Fe-, Co-, and Ni-doped BCZT ceramics in Figure 5C-E exhibit S-type hysteretic *M–H* curves with non-zero remanent magnetization (M_r) and coercive field (H_c), indicating the existence of ferromagnetic long-range ordering. The M_r, H_c, and saturation magnetization (M_s) values of the BCZT ceramics are displayed in Table 2. It can be observed that the Fe-doped BCZT presents a larger saturation magnetization and a smaller coercive field than the others, indicative of typical ferromagnetism.

In the BCZT material, as the *d* orbitals of Ti^{4+} and Zr^{4+} ions are in the d^0 states and they are not magnetic,[41] the magnetism is derived from the doping ions. This magnetic behavior can be explained by the F-center exchange mechanism proposed by Coey et al[42] in Fe-doped SnO_2 films. Considering Fe-doped BCZT as an example, the grain size reduction demonstrates that oxygen vacancies (V_O^{2-}) are generated in the lattice to offset the charge imbalance caused by the substitution of Fe^{3+} for Ti^{4+}. An electron is captured by an oxygen vacancy to form an F center, where the orbital occupied by the electron will overlap with the 3*d* orbitals of two adjacent Fe^{3+} ions as shown in Figure 5F. The ferromagnetic exchange coupling interaction between the magnetic Fe^{3+} ions and the oxygen vacancies will facilitate the formation of Fe^{3+}–V_O^{2-}–Fe^{3+} groups. The outer shell electron configuration of Fe^{3+} ions is $3d^5$ with five unoccupied minority spin orbitals. The captured electron will spin down, and the two adjacent Fe^{3+} ions will spin up. Consequently, the F center is akin to a bound magnetic polaron and exhibits an external magnetic moment, thereby leading to ferromagnetic coupling in BCZT ceramics. By contrast, the outer shell electron configuration of Co^{2+} is $3d^7$ with three unoccupied orbitals, whereas that of Ni^{2+} is $3d^8$ with two unoccupied orbitals. Therefore, Ni^{2+} ions have the fewest fillable electrons, generate the smallest magnetic

moment, and exhibit the lowest magnetization intensity, followed by Co^{2+} and Fe^{3+}. Notably, the optical absorbance and magnetic property of BCZT can be modified simultaneously via Fe and Co doping. In addition, as the exchange coupling interaction between the TM cations and oxygen is inherently antiferromagnetic,[43] the *M-H* curve is approximately linear in a macroscopic view, which indicates that the dopant concentration needs to be further optimized.

4 | CONCLUSIONS

In summary, the influence of TM doping on the microstructural phase evolution, band gap modulation, and magnetic properties of BCZT ceramics has been investigated in detail. XRD and Raman analyses reveal that TM-doped BCZT ceramics present a rhombohedral phase rather than the coexisting rhombohedral and tetragonal phases presented by pure BCZT. SEM images further demonstrate the grain refinement owing to TM doping. Significant modification of the optical and magnetic properties has been observed in all the TM-doped BCZT ceramics. The band gap of Co-doped BCZT is significantly reduced from 3.18 to 1.68 eV. Moreover the exchange coupling interactions between the TM cations and oxygen vacancies are confirmed to induce the ferromagnetic order in Fe-doped BCZT. These results indicate that BCZT lead-free ceramics are promising for application in photovoltaic cells and multifunctional devices.

ORCID

Yuemin Zhang https://orcid.org/0000-0002-5814-0167

REFERENCES

1. Khomskii D. Classifying multiferroics: mechanisms and effects. Physics. 2009;2:20.
2. Fiebig M, Lottermoser T, Meier D, Trassin M. The evolution of multiferroics. Nat Rev Mater. 2016;1(8):16046.
3. Shimada T, Uratani Y, Kitamura T. Vacancy-driven ferromagnetism in ferroelectric $PbTiO_3$. Appl Phys Lett. 2012;100:162901.

4. Park K-I, Son JH, Hwang G-T, Jeong CK, Ryu J, Koo M, et al. Highly-efficient, flexible piezoelectric PZT thin film nanogenerator on plastic substrates. Adv Mater. 2014;26(16):2514–20.

5. Jeong CK, Cho SB, Han JH, Park DY, Yang S, Park K-I, et al. Flexible highly-effective energy harvester via crystallographic and computational control of nanointerfacial morphotropic piezoelectric thin film. Nano Res. 2017;10(2):437–55.

6. Reddy SR, Prasad VVB, Bysakh S, Shanker V, Joardar J, Roy SK. Ferroelectric and piezoelectric properties of $Ba_{0.85}Ca_{0.15}Ti_{0.90}Zr_{0.10}O_3$ films in 200 nm thickness range. J Am Ceram Soc. 2019;102:1277–86.

7. Hreščak J, Bencan A, Rojac T, Malič B. The influence of different niobium pentoxide precursors on the solid-state synthesis of potassium sodium niobate. J Eur Ceram Soc. 2013;33(15–16):3065–75.

8. Xu C, Lin D, Kwok KW. Structure, electrical properties and depolarization temperature of $(Bi_{0.5}Na_{0.5})TiO_3$-$BaTiO_3$ lead-free piezoelectric ceramics. Solid State Sci. 2008;10(7):934–40.

9. Zhang Y, Sun H, Chen W. A brief review of $Ba(Ti_{0.8}Zr_{0.2})O_3$-$(Ba_{0.7}Ca_{0.3})TiO_3$ based lead-free piezoelectric ceramics: past, present and future perspectives. J Phys Chem Solids. 2018;114:207–19.

10. Liu W, Ren X. Large piezoelectric effect in Pb-free ceramics. Phys Rev Lett. 2009;103(25):230–5.

11. Sun H, Duan S, Liu X, Wang D, Sui H. Lead-free $Ba_{0.98}Ca_{0.02}Zr_{0.02}Ti_{0.98}O_3$ ceramics with enhanced electrical performance by modifying MnO_2 doping content and sintering temperature. J Alloys Compd. 2016;670:262–7.

12. Jaimeewong P, Sittinon S, Buntham S, Bomlai P, Namsar O, Pojprapai S, et al. Ferroelectric, piezoelectric and dielectric behaviors of CoO- and Fe_2O_3-doped BCZT ceramics. Phys Status Solidi A. 2018;215(20):1701023.

13. Wang Z, Wang J, Chao X, Wei L, Yang B, Wang D, et al. structure, dielectric, piezoelectric, and energy storage performance of $(Ba_{0.85}Ca_{0.15})(Ti_{0.9}Zr_{0.1})O_3$ ceramics prepared by different methods. J Mater Sci Mater Electron. 2016;27(5):5047–58.

14. Li W, Zhou D, Xu R, Wang D, Su J, Pang L, et al. $BaTiO_3$-based multilayers with outstanding energy storage performance for high temperature capacitor applications. ACS Appl Energy Mater. 2019;2(8):5499–506.

15. Liu G, Li Y, Shi M, Yu L, Chen P, Yu K, et al. An investigation of the dielectric energy storage performance of $Bi(Mg_{2/3}Nb_{1/3})O_3$-modifed $BaTiO_3$ Pb-free bulk ceramics with improved temperature/frequency stability. Ceram Int. 2019;45(15):19189–96.

16. Yuan Y, Xiao Z, Yang B, Huang J. Arising applications of ferroelectric materials in photovoltaic devices. J Mater Chem A. 2014;2(17):6027–41.

17. Zhou W, Deng H, Yu L, Yang P, Chu J. Magnetism switching and band-gap narrowing in Ni-doped $PbTiO_3$ thin films. J Appl Phys. 2015;117(19):194102.

18. Choi T, Lee S, Choi YJ, Kiryukhin V, Cheong SW. Switchable ferroelectric diode and photovoltaic effect in $BiFeO_3$. Science. 2009;324(5923):63–6.

19. Wang T, Deng H, Meng X, Cao H, Zhou W, Shen P, et al. Tunable polarization and magnetization at room-temperature in narrow bandgap Aurivillius $Bi_6Fe_{2-x}Co_{x/2}Ni_{x/2}Ti_3O_{18}$. Ceram Int. 2017;43(12):8792–9.

20. Ma C, Wang X, Gan Z, Tan W, Wang X, Zhang J, et al. Photoluminescence and optical temperature sensing in Sm^{3+}-doped $Ba_{0.85}Ca_{0.15}Ti_{0.90}Zr_{0.10}O_3$ lead-free ceramics. Ceram Int. 2019;45(1):588–94.

21. Bennett JW, Grinberg I, Rappe AM. New highly polar semiconductor ferroelectrics through d^8 cation-O vacancy substitution into $PbTiO_3$: a theoretical study. J Am Chem Soc. 2008;130(51):17409–12.

22. Zheng T, Deng H, Zhou W, Yang P, Chu J. Optical bandgap reduction and ferromagnetic enhancement at room-temperature in $PbTi_{1-x}Fe_xO_{3-\delta}$ ferroelectrics. Mater Lett. 2016;185:380–3.

23. Yu L, Deng H, Zhou W, Zhang Q, Yang P, Chu J. Effects of (Sm, Mn and Ni) co-doping on structural, optical and magnetic properties of $BiFeO_3$ thin films fabricated by a sol-gel technique. Mater Lett. 2016;170:85–8.

24. Luo B, Wang X, Wang Y, Li L. Fabrication, characterization, properties and theoretical analysis of ceramic/PVDF composite flexible films with high dielectric constant and low dielectric loss. J Mater Chem A. 2014;2(2):510–9.

25. Zhao C, Wang H, Xiong J, Wu J. Composition-driven phase boundary and electrical properties in $(Ba_{0.94}Ca_{0.06})(Ti_{1-x}M_x)O_3$ (M = Sn, Hf, Zr) lead-free ceramics. Dalton Trans. 2016;45(15):6466–80.

26. Tsur Y, Dunbar TD, Randall CA. Crystal and defect chemistry of rare earth cations in $BaTiO_3$. J Electroceramics. 2001;7(1):25–34.

27. Wu W, Cheng LI, Bai S, Dou W, Xu QI, Wei Z, et al. Electrospinning lead-free $0.5Ba(Zr_{0.2}Ti_{0.8})O_3$–$0.5(Ba_{0.7}Ca_{0.3})TiO_3$ nanowires and their application in energy harvesting. J Mater Chem A. 2013;1(25):7332–8.

28. Wu J, Xiao D, Wu W, Chen Q, Zhu J, Yang Z, et al. Role of room-temperature phase transition in the electrical properties of (Ba, Ca)(Ti, Zr)O_3 ceramics. Scr Mater. 2011;65(9):771–4.

29. Begg BD, Finnie KS, Vance ER. Raman study of the relationship between room-temperature tetragonality and the curie point of barium titanate. J Am Ceram Soc. 2005;79(10):2666–72.

30. Yang Y, Zhou Y, Ren J, Zheng Q, Lam KH, Lin D. Phase coexistence and large piezoelectricity in $BaTiO_3$-$CaSnO_3$ lead-free ceramics. J Am Ceram Soc. 2018;101(6):2594–605.

31. Phan TL, Thang PD, Ho TA, Manh TV, Thanh TD, Lam VD, et al. Local geometric and electronic structures and origin of magnetism in Co-doped $BaTiO_3$ multiferroics. J Appl Phys. 2015;117(17):17D904.

32. Venkata RE, Mahajan A, Graça MPF, Mendiratta SK, Monteiro JM, Valente MA. Structure and ferroelectric studies of $(Ba_{0.85}Ca_{0.15})(Ti_{0.9}Zr_{0.1})O_3$ piezoelectric ceramics. Mater Res Bull. 2013;48(10):4395–401.

33. Park JH, Jang HM, Kim HS, Park CG, Lee SG. Strain-mediated magnetoelectric coupling in $BaTiO_3$ -Co nanocomposite thin films. Appl Phys Lett. 2008;92(6):062908.

34. Shi L, Zhang B, Liao Q, Zhu L, Zhao L, Zhang D, et al. Piezoelectric properties of Fe_2O_3 doped $BiYbO_3$-Pb(Zr, Ti)O_3 high Curie temperature ceramics. Ceram Int. 2014;40(8):11485–91.

35. Zhou W, Deng H, Yu L, Yang P, Chu J. Band-gap narrowing and magnetic behavior of Ni-doped $Ba(Ti_{0.875}Ce_{0.125})O_3$ thin films. J Phys D Appl Phys. 2015;48(45):455308.

36. Tauc J, Grigorovici R, Vancu A. Optical properties and electronic structure of amorphous germanium. Phys Status Solidi. 1966;15(2):627–37.

37. Pascual-Gonzalez C, Schileo G, Murakami S, Khesro A, Wang D, Reaney IM, et al. Continuously controllable optical band gap in orthorhombic ferroelectric $KNbO_3$-$BiFeO_3$ ceramics. Appl Phys Lett. 2017;110(17):172902.

38. Pascual-Gonzalez C, Schileo G, Khesro A, Sterianou I, Wang D, Reaney IM, et al. Band gap evolution and a piezoelectric-to-electrostrictive crossover in $(1–x)KNbO_3$-$x(Ba_{0.5}Bi_{0.5})(Nb_{0.5}Zn_{0.5})O_3$ ceramics. J Mater Chem C. 2017;5(8):1990–6.

39. Chen X, Huang F, Lu Z, Xue Y, Min J, Li J, et al. Influence of transition metal doping (X = Mn, Fe Co, Ni) on the structure and bandgap of ferroelectric $Bi_{3.15}Nd_{0.85}Ti_2X_1O_{12}$. J Phys D Appl Phys. 2017;50(10):105104.

40. Choi WS, Lee HN. Strain tuning of electronic structure in $Bi_4Ti_3O_{12}$-$LaCoO_3$ epitaxial thin films. Phys Rev B. 2015;91(17):174101.

41. Wang F, Grinberg I, Rappe AM. Band gap engineering strategy via polarization rotation in perovskite ferroelectrics. Appl Phys Lett. 2014;104(15):152903.

42. Coey JMD, Douvalis AP, Fitzgerald CB, Venkatesan M. Ferromagnetism in Fe-doped SnO_2 thin films. Appl Phys Lett. 2004;84(8):1332–4.

43. Ren Z, Xu G, Wei X, Liu Y, Hou X, Du P, et al. Room-temperature ferromagnetism in Fe-doped $PbTiO_3$ nanocrystals. Appl Phys Lett. 2007;91(6):063106.